Letter

Photoinduced Negative Differential Resistance at a Graphene/Silicon Interface: A Nonadiabatic Quantum Molecular Dynamics Study

Hinata Hokyo, Kai Ito, Rajiv K. Kalia, Rehan Kapadia, Aiichiro Nakano,* Kohei Shimamura,* Fuyuki Shimojo, and Priya Vashishta

Cite This: *J. Phys. Chem. Lett.* 2024, 15, 9226−9232

Read Online

ACCESS | Metrics & More | Article Recommendations | Supporting Information

ABSTRACT: The oscillatory retinal neuron (ORN) is a promising technology for achieving in-sensor cognitive image computing without external power. While its operation is based on photoinduced negative differential resistance (NDR) at a graphene/silicon interface to directly convert the incident optical signal into voltage oscillations, the optoelectronic mechanism of the NDR remains elusive. Here, nonadiabatic quantum molecular dynamics simulations show that the interplay of band alignment and charge transfer rates of photoexcited carriers at varying applied voltages gives rise to NDR at a graphene/silicon interface under illumination. Such intrinsic NDR at an interface, along with extrinsic circuit-level factors, could enable the much needed rational design of desired image computing functionality of ORN devices in the era of ubiquitous AI on edge devices.
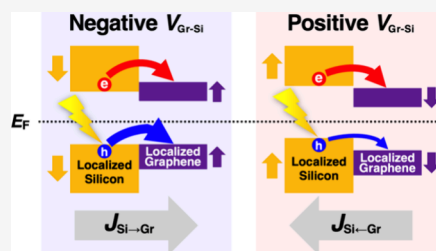
Negative differential resistance (NDR) is characterized by a nonlinear relationship between the applied voltage and electrical current, deviating from the typical linear behavior.[1] Initially observed in germanium diodes (for which Leo Esaki received the Nobel Prize in Physics in 1973),[2] NDR has been found across a wide range of materials, including semiconductors and organic biomaterials, finding widespread utilization in various electronic devices such as oscillators, memory devices, and high-speed switching devices.[3] Recently, NDR has been demonstrated in systems comprising stacked graphene and silicon, where particularly notable is the increased current under reverse bias under illumination.[4,5] This photoinduced NDR gives rise to voltage oscillations even at zero applied voltage solely driven by incident light, thereby realizing novel oscillatory retinal neuron (ORN) devices that are capable of in-sensor cognitive image computing without external power sources.[4] In an ORN, a light detector demonstrating NDR under illumination is coupled with an inductive element to drive electrical oscillations, leveraging dynamical instability associated with NDR. The fundamental scientific question underlying an ORN is how light induces NDR at a graphene/silicon interface.

Often, the NDR phenomenon is not associated with a single physical mechanism,[6] making it difficult to identify key factors responsible for it. Nevertheless, quantum mechanical calculations have played an important role in elucidating such intricate mechanisms. Theoretical studies utilizing density functional theory (DFT) and nonequilibrium Green's function have predicted NDR characteristics in graphene, indicating its potential for device applications.[7,8] On the basis of the energy

band theory, it is possible to attain NDR through the stacking of semiconductors with varied band alignments.[9−11]

Even more challenging is photoinduced NDR, which requires an understanding of photoexcited carrier dynamics, including charge transfer (CT) at interfaces.[12] Here, nonadiabatic quantum molecular dynamics (NAQMD) simulations[13−15] are indispensable, by describing photoexcitation dynamics involving electrons and nuclei from first principles in the framework of time-dependent DFT (TDDFT) and nonadiabatic coupling between electrons and nuclei. To elucidate the mechanisms underlying photoinduced NDR in an ORN,[4] NAQMD can directly track far-from-equilibrium dynamics of photoexcited electrons and holes coupled with nuclei, thereby providing microscopic insights into optoelectronic mechanisms under illumination.[16−18] To represent an applied voltage in experiments,[4] we apply an electric field in NAQMD simulations using Berry-phase[19] and double-cell[20] methods.[21] By applying these methods to a graphene sheet stacked on a silicon surface, we elucidate the electronic mechanisms underlying the experimentally observed photoinduced NDR in ORN devices.[4] NAQMD simulation results exhibit photoinduced nonlinear current−voltage characteristics

9226
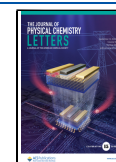
indicative of NDR, and we find it primarily governed by interfacial CT of hole carriers through detailed analysis of band alignment at varying applied voltages. While the experimentally observed photoinduced NDR in ORN devices[4] is influenced by a number of circuit-level factors such as metals like Ti and Au and oxides like SiO_2, this study demonstrates the existence of intrinsic photoinduced NDR at a graphene/silicon interface, which will likely play an important role in the rational design of future ORN devices.

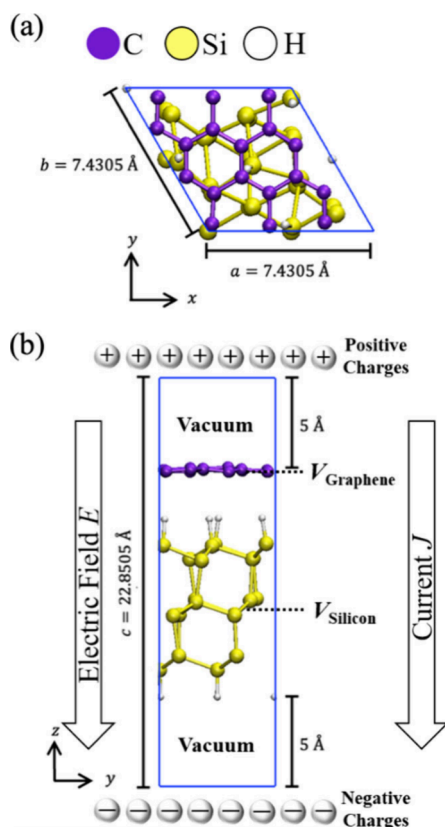Figure 1 illustrates the simulated graphene/silicon system, in which a graphene sheet is stacked on a stable (111) surface[22]

Figure 1. (a) Top and (b) side views of the initial atomic configuration of the simulated graphene/silicon system. The purple, yellow, and white spheres represent carbon, silicon, and hydrogen atoms, respectively. In panel b, the directions of a positive electric field E and a positive current J are denoted by arrows, whereas the positions to measure the potential of graphene ($V_{Graphene}$) and that of silicon ($V_{Silicon}$) are labeled. Also shown are positive and negative charge sheets at the top and bottom edges of the system, respectively, to generate an external electric field, which corresponds to an external power source in experiments.

of silicon crystal (see Methods for details). The dangling bonds on the Si surfaces are terminated with hydrogen atoms. Starting with this configuration, we first perform adiabatic quantum molecular dynamics (QMD) simulations[23] at a temperature of 300 K for structural relaxation. We then apply electric field E in the surface-normal (or Cartesian z) direction with varying strengths ranging from negative to positive. The direction of a positive electric field is defined as shown in Figure 1b, i.e., pointing from graphene to silicon. For each field strength, we further run a QMD simulation until steady states are reached. We sample multiple atomic configurations from each steady QMD simulation trajectory to initiate multiple

NAQMD simulations to study the photoexcitation at each field strength. We consider six field strengths, including zero electric field, and perform 29 NAQMD simulations to accumulate statistics for each field strength. Instead of the electric-field strength, we will hereafter use the corresponding potential difference, V_{Gr-Si} ($=V_{Graphene} - V_{Silicon}$), between graphene and silicon as shown in Figure 1b (see section 1 of the Supporting Information for details). Here, $V_{Graphene}$ and $V_{Silicon}$ are the potential values of graphene and silicon, respectively. The applied voltage induces electric current J, the positive direction of which is also defined in Figure 1b, i.e., pointing from graphene to silicon.

In each NAQMD simulation, one electron is excited from the highest-energy state that is localized in silicon within the valence band (VB) to the lowest-energy state that is also localized in silicon within the conduction band (CB) at time zero, because light is absorbed by the silicon substrate in experiments to generate excited electrons and holes.[4] In fact, the wavelength of light in the ORN experiment was 445 nm,[4] and the corresponding photon energy of 2.79 eV is much larger than the band gap of silicon, thus generating a large number of carriers in silicon. We also note that the number of photocarriers in graphene is much smaller due to the large difference in volume between the graphene monolayer and bulk silicon substrate. In the NAQMD simulation, electric current is characterized by charge transfer (CT) of the excited electron or hole from silicon to graphene. To do so, the occupancies of each electronic state in silicon and graphene are calculated by Mulliken analysis.[24] The VB and CB states for initial photoexcitation are selected such that their occupancy in silicon is >95%. We quantify CT throughout the NAQMD simulation by following the time evolution of the occupancies of the electron and hole.

Figure 2 shows the time evolution of Kohn−Sham eigen-energies around the Fermi energy in one of the NAQMD simulations under an electric field E of −0.0003125 a.u. (the corresponding V_{Gr-Si} = −0.12 V). The figure illustrates how charge carriers transfer from silicon to graphene, where VBM-n denotes the nth highest-energy Kohn−Sham state below the valence band maximum (VBM) and CBM-n denotes the nth lowest-energy Kohn−Sham state above the conduction band maximum (CBM). At time zero, one electron is excited from the highest-energy VB state that is localized in silicon (VBM-1) to the lowest-energy CB state that is also localized in silicon (CBM+2) to simulate photoexcitation of an electron−hole pair in silicon (see the left panel of Figure 2). For the hole on the VB side (colored blue), there exists a graphene-localized occupied state, VBM, whose eigenvalue (ε_{VBM}) is very close to that of VBM-1 (ε_{VBM-1}). Consequently, the hole in the VBM rapidly undergoes a transition to one of these graphene-localized occupied states at 29 fs. It is also important to note that the electrostatic energy due to the electric field facilitates the transfer of the hole from silicon to graphene. For the electron on the CB side (colored red), there are two graphene-localized unoccupied states, CBM and CBM+1. Because their eigenvalues (ε_{CBM} and ε_{CBM+1}) are somewhat far from that of CBM+2 (i.e., the excited electron), ε_{CBM+2}, it takes longer (72 fs) for the excited electron to undergo a transition to one of these graphene-localized unoccupied states. This electron transfer is assisted by the change in Kohn−Sham energies that reflects the relaxation by atomic movements, bringing ε_{CBM} and ε_{CBM+1} closer to ε_{CBM+2}. However, the electric field acts to hinder the transfer of the electron from silicon to
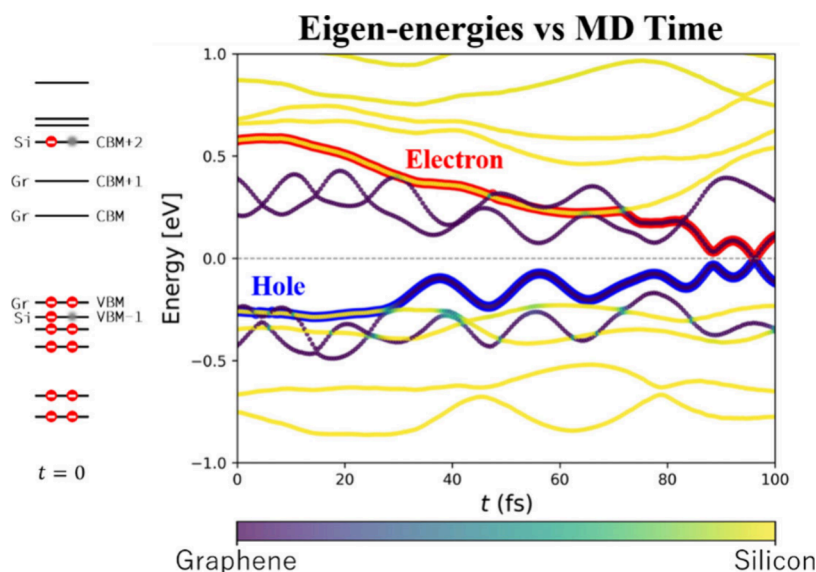
Figure 2. Time evolution of Kohn−Sham eigen-energies in a NAQMD simulation with an electric field of −0.0003125 a.u. Here, the energy is measured relative to the Fermi energy. At time zero, one electron is excited from the VBM to CBM+2 (left). The excited electron and hole states are colored red and blue, respectively. In addition, the occupancy of each state in silicon and graphene is color-coded.

graphene. In this simulation, the hole underwent a transition to the localized states in graphene more quickly than the excited electron, which indicates that a negative current can easily flow from silicon to graphene (i.e., $-J$ direction in Figure 1b). Namely, hole energy $\varepsilon_{\mathrm{VBM-1}}$ is closer to other VB-state energies (also to the Fermi energy) than electron energy $\varepsilon_{\mathrm{CBM+2}}$ is to other CB-state energies and the Fermi energy at time zero, resulting in more rapid CT of the hole than of the electron. This observation suggests the key factors involved in rapid CT of carriers. It is easy to understand that the electrostatic energy felt by the carriers due to the applied electric field controls the CT rate. In addition, there are other important factors. The eigenvalues of the photoexcited hole and electron states in silicon at time zero are mixed with those of the graphene-localized states, and they are close to the Fermi energy. Because the alignment of silicon and graphene electronic bands is shifted by the applied electric field, we naturally expect the resulting change in electron and hole CT rates, which accordingly modifies the change in the electric current. Such rapid decay of photoexcited carriers to the CB/VB edges makes hot carrier effects rather inappreciable.

The example presented above suggests an electronic mechanism underlying photoinduced current at the graphene/silicon interface, which can be characterized by the time for photoexcited electrons and holes to transfer from silicon to graphene. Because the NAQMD method stochastically determines the transition between electronic states, it is necessary to take sufficient statistics for the transfer time. We thus perform 29 NAQMD simulations with different initial atomic configurations for each electric field. We define the inverse of the CT time for the excited electron or hole as the CT rate and then calculate the average CT rates, $r_{\mathrm{elec}}^{\mathrm{CT}}$ and $r_{\mathrm{hole}}^{\mathrm{CT}}$, of the excited electron and hole, respectively, over the 29 simulations. The calculation procedure for the CT rates is discussed in section 2 of the Supporting Information. A finite $r_{\mathrm{elec}}^{\mathrm{CT}}$ value signifies a positive current due to the flow of the excited electron in the direction of J shown in Figure 1b. On the contrary, a finite $r_{\mathrm{hole}}^{\mathrm{CT}}$ value signifies a negative current due to the flow of the hole (i.e., $-J$ direction in Figure 1b). As such,

we use their differences, $r_{\mathrm{elec}}^{\mathrm{CT}}$ and $r_{\mathrm{hole}}^{\mathrm{CT}}$, as a proxy of electrical current along the direction of the electric field.

Figure 3 shows the calculated CT rates as a function of $V_{\mathrm{Gr-Si}}$, where the red and blue lines represent $r_{\mathrm{elec}}^{\mathrm{CT}}$ and $r_{\mathrm{hole}}^{\mathrm{CT}}$,
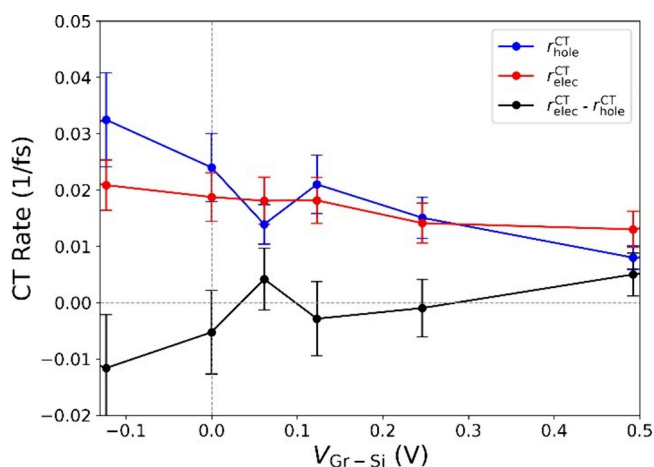

Figure 3. Potential difference $V_{\mathrm{Gr-Si}}$-dependent average charge transfer (CT) rates of the excited electron ($r_{\mathrm{elec}}^{\mathrm{CT}}$, red), hole ($r_{\mathrm{hole}}^{\mathrm{CT}}$, blue), and the difference ($r_{\mathrm{elec}}^{\mathrm{CT}} - r_{\mathrm{hole}}^{\mathrm{CT}}$, black). The error bars represent the standard errors calculated over 29 NAQMD simulations. The calculation details are described in section 1 of the Supporting Information.

respectively, while the black line represents their difference, $r_{\mathrm{elec}}^{\mathrm{CT}} - r_{\mathrm{hole}}^{\mathrm{CT}}$. The error bars are calculated following the procedure discussed in section 2 of the Supporting Information. Overall, both $r_{\mathrm{elec}}^{\mathrm{CT}}$ and $r_{\mathrm{hole}}^{\mathrm{CT}}$ decrease as a function of $V_{\mathrm{Gr-Si}}$, where the decrease in $r_{\mathrm{hole}}^{\mathrm{CT}}$ is larger than that of $r_{\mathrm{elec}}^{\mathrm{CT}}$. Conversely, electric current J represented by $r_{\mathrm{elec}}^{\mathrm{CT}} - r_{\mathrm{hole}}^{\mathrm{CT}}$ exhibits an overall increase as a function of $V_{\mathrm{Gr-Si}}$. We did not observe NDR in the negative voltage region seen in the experiment.[4] However, interestingly, our simulation results show that $r_{\mathrm{elec}}^{\mathrm{CT}} - r_{\mathrm{hole}}^{\mathrm{CT}}$ as a function of $V_{\mathrm{Gr-Si}}$ in the positive voltage region has a peak at a $V_{\mathrm{Gr-Si}}$ of 0.06 V. This indicates
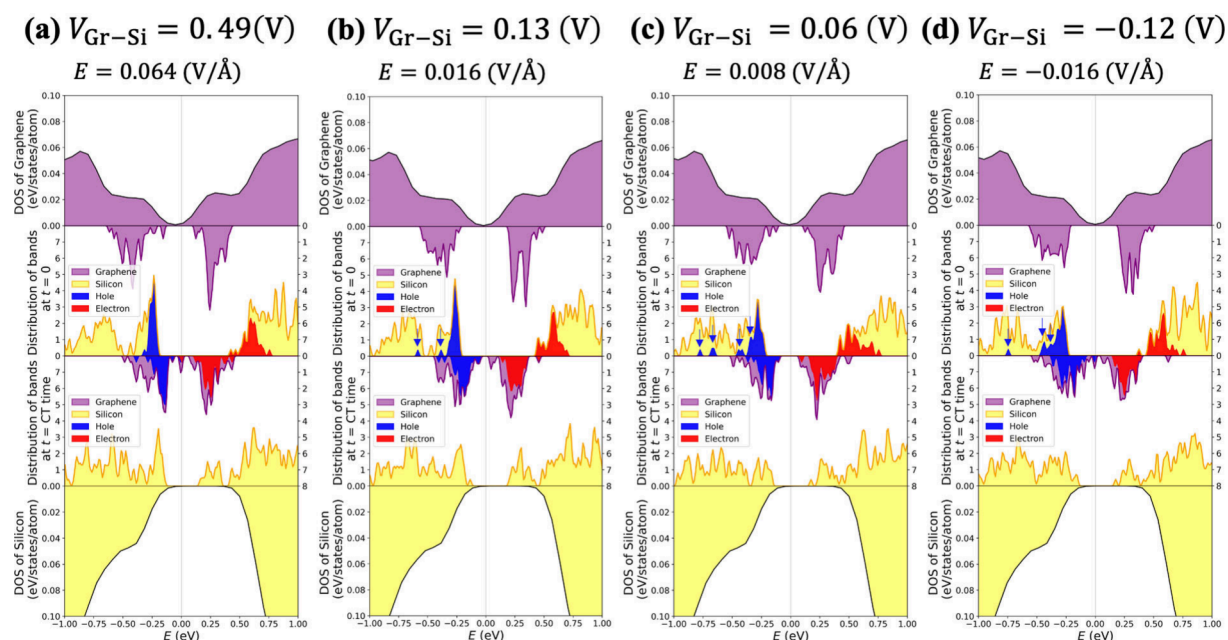
Figure 4. Partial density of states (DOS) of graphene (top panels) and silicon (bottom panels) at $V_{\text{Gr-Si}}$ values of (a) 0.49, (b) 0.13, (c) 0.06, and (d) −0.12 V. The corresponding electric-field strengths are also shown. The middle panels show distributions of localized Kohn−Sham states within graphene (purple) and silicon (yellow) at time zero and CT time over 29 NAQMD simulations. Also shown are distributions of hole (blue) and excited electron (red) states at time zero and CT time. For the hole distribution at time zero, small peaks other than the main one are highlighted by blue arrows.

that our NAQMD simulation captures the essence of NDR at a graphene/silicon interface, and the elucidation of its mechanism would help understand experimentally observed NDR.[4] Noting the rather featureless $r_{\text{elec}}^{\text{CT}}$−$V_{\text{Gr-Si}}$ curve, we can conclude that NDR predominantly arises from the $r_{\text{hole}}^{\text{CT}}$−$V_{\text{Gr-Si}}$ relationship. Namely, the behavior of holes in response to electric fields holds the key for elucidating the mechanism of NDR.

To elucidate the electronic mechanism underlying the nonlinear NDR behavior of $r_{\text{elec}}^{\text{CT}} - r_{\text{hole}}^{\text{CT}}$ in Figure 3, we analyze the variation of Kohn−Sham eigen-energies around the Fermi energy for the 29 NAQMD simulations, like what we did for Figure 2. NAQMD simulations provide information about the electronic states localized in silicon or graphene as well as the excited electron and hole states at each time instance. We draw the distributions of the Kohn−Sham eigen-energies at time time zero and the time at which CT occurs ($t = t^{\text{CT}}$) in the 29 NAQMD simulations. Figure 4 shows these distributions at $V_{\text{Gr-Si}}$ values of (a) 0.49, (b) 0.13, (c) 0.06, and (d) −0.12 V, in addition to the partial density of states (DOS) for graphene and silicon calculated from the QMD simulation. The distributions at other $V_{\text{Gr-Si}}$ values are shown in Figure S4. As $V_{\text{Gr-Si}}$ decreases, the partial DOS of graphene shifts toward a higher energy while that of silicon moves to a lower energy. These shifts affect $r_{\text{elec}}^{\text{CT}} - r_{\text{hole}}^{\text{CT}}$. First, let us examine why $r_{\text{elec}}^{\text{CT}} - r_{\text{hole}}^{\text{CT}}$ is positive at a $V_{\text{Gr-Si}}$ of 0.49 V as shown in Figure 4a. Focusing on the excited electron's behavior due to the band energy shift, we found that the position of the excited electron's distribution at time zero is much higher (∼0.5 eV) than the localized states of graphene in the CB, away from the Fermi energy, which tends to delay CT to graphene. However, the largest positive electric field ($E = 0.00125$ a.u.) still leads to a rapid CT (i.e., a large $r_{\text{elec}}^{\text{CT}}$), despite this energy band shift. On the contrary, for the hole, CT to graphene should be strongly hindered by such a large electric field from graphene to silicon.

Nevertheless, $r_{\text{hole}}^{\text{CT}}$ does not become too small, likely because the distributions of holes and graphene-localized states are much closer to each other compared to those for the excited electron. In this way, $r_{\text{elec}}^{\text{CT}} - r_{\text{hole}}^{\text{CT}}$ takes a positive value through the nontrivial relationship between the electric-field strength and the alignment of the bands. Next, in Figure 3, as $V_{\text{Gr-Si}}$ decreases, $r_{\text{hole}}^{\text{CT}}$ becomes larger than $r_{\text{elec}}^{\text{CT}}$; at a $V_{\text{Gr-Si}}$ of 0.13 V (i.e., $E = 0.0003125$ a.u.), $r_{\text{hole}}^{\text{CT}}$ is clearly larger than $r_{\text{elec}}^{\text{CT}}$. As shown in Figure 4b, the localized states in graphene are mixed with the main peak of the hole distribution at time zero, resulting in a higher $r_{\text{hole}}^{\text{CT}}$ even inhibited by the electric field from graphene to silicon. The excited electron localized in silicon at time zero is quite weakly mixed with the states localized in graphene in the CB, despite a driving force from the electric field, providing a smaller $r_{\text{elec}}^{\text{CT}}$.

However, at a $V_{\text{Gr-Si}}$ of 0.06 V (i.e., $E = 0.00015625$ a.u.) as shown in Figure 4c, $r_{\text{hole}}^{\text{CT}}$ becomes smaller than $r_{\text{elec}}^{\text{CT}}$, even though the mixing between the local states of graphene and the main peak position of the hole distribution at time zero is further intensified and an electric-field strength weaker than that at a $V_{\text{Gr-Si}}$ of 0.13 V is given. This change in $r_{\text{hole}}^{\text{CT}}$ is the key to understanding the NDR phenomenon observed in this study. As mentioned above, the locations of the main peaks of the hole distributions at time zero for $V_{\text{Gr-Si}}$ values of both 0.13 and 0.06 V appear to be mixed with the distributions of graphene-localized states. However, other than the main peaks, the numbers of the smaller peaks (the blue arrows denote the hole distributions at time zero in Figure 4), located between −0.75 and −0.4 eV, are different at $V_{\text{Gr-Si}}$ values of 0.13 and 0.06 V, and there are fewer peaks at 0.13 V than at 0.06 V. Because the farther the hole is from the Fermi energy, the longer it takes to transfer toward graphene as shown in Figure 2, $r_{\text{hole}}^{\text{CT}}$ at 0.06 V becomes smaller. Moreover, the number of small peaks tends to decrease in the $V_{\text{Gr-Si}}$ range of 0.13−0.49 V as opposed to the higher-voltage range (Figure 3 and Figure

S4), giving the possibility of a large $r_{\text{hole}}^{\text{CT}}$ against the electric field toward silicon. The reason for the appearance and disappearance of the small peaks may be attributed to the nontrivial shift in band energy due to the given electric field, which is considered to be associated with the increase in $r_{\text{elec}}^{\text{CT}} - r_{\text{hole}}^{\text{CT}}$ at a $V_{\text{Gr-Si}}$ of 0.06 V. Finally, the excited electron and hole states at a $V_{\text{Gr-Si}}$ of −0.12 V (Figure 4d) are similar to those at a $V_{\text{Gr-Si}}$ of 0.06 V, but the negative electric field ($E = -0.0003125$ a.u.) facilitates large CT of the hole and conversely inhibits that of the excited electron. Hence, $r_{\text{elec}}^{\text{CT}} - r_{\text{hole}}^{\text{CT}}$ is smaller than that at a $V_{\text{Gr-Si}}$ of 0.06 V.

In addition to CT, charge recombination (CR) of the photoexcited electron and hole at a graphene/silicon interface also influences the photocurrent.[4] NAQMD simulations can also provide the CR time, at which hole−excited electron pairs are annihilated, and the CR rate as its inverse. The CR rate as a function of $V_{\text{Gr-Si}}$ is shown in Figure S6; details of the CR calculation are given in section 4 of the Supporting Information. The CR rate is smaller than $r_{\text{elec}}^{\text{CT}}$ and $r_{\text{hole}}^{\text{CT}}$ and is roughly constant with respect to $V_{\text{Gr-Si}}$. In other words, the CR rate is rather insensitive to $V_{\text{Gr-Si}}$. Consequently, the overall NDR characteristic is dictated by CT rates, instead of CR rates.

In summary, we used QMD and NAQMD simulations to identify optoelectronic mechanisms of NDR at a graphene/silicon interface under illumination. We characterized the behavior of photoexcited carriers using NAQMD simulations in which an electric field was applied to the stacked graphene/silicon system. It was found that CT rates of photoexcited electrons and holes, $r_{\text{elec}}^{\text{CT}} - r_{\text{hole}}^{\text{CT}}$, representing photocurrent exhibit NDR. Our analysis revealed distinct shifts in the energy bands of graphene and silicon with varying electric fields. The observed NDR in the $V_{\text{Gr-Si}}$ dependence of $r_{\text{elec}}^{\text{CT}} - r_{\text{hole}}^{\text{CT}}$ was found to be dictated by the distributions of excited electrons and holes, those of localized bands in graphene and silicon, and the applied voltage, primarily governed by the interfacial CT of hole carriers. These findings, along with other NDR mechanisms in 2D materials,[25] shed light on the intricate interplay among the electronic properties of graphene/silicon devices, offering valuable insights for the design and optimization of future ultra-low-power electronic components based ORN in the era of ubiquitous AI on edge devices. It should be noted that experimentally observed NDR[4] is influenced by many other factors such as metals and oxides, in addition to the photoinduced NDR intrinsic to a graphene/silicon interface. Future studies would include those factors for more quantitative comparison with experiments. Furthermore, we plan to apply our approach to graphene/germanium systems. Epitaxial graphene on various germanium surfaces may exhibit interesting interfacial CT not seen with silicon. The smaller band gap of germanium would also lead to possibilities in the short-wave infrared regime, which is an area of great interest for many applications.

■ METHODS

QMD and NAQMD Methods. We perform both adiabatic QMD and NAQMD simulations using the QXMD software.[26] A QMD simulation[23] follows the trajectories of all atoms, while calculating interatomic forces quantum mechanically from first principles within the framework of DFT.[27,28] Adiabatic QMD assumes that electrons remain in the ground state throughout the simulation.[23] The electronic states are calculated using the projector-augmented wave (PAW) method,[29,30] where projector functions are generated for $3s^2 3p^2 3d^0$ for silicon, $2s^2 2p^2$ for

carbon, and $1s^1$ for hydrogen atoms. The generalized gradient approximation (GGA) is used for the exchange-correlation functional.[31] The plane-wave cutoff energies are set at 20 Ry for wave functions and 180 Ry for the electron density. Brillouin zone sampling is performed at the Γ point during the QMD simulation. To compute the electronic partial density of states (DOS) of graphene and silicon, we instead use $10 \times 10 \times 1$ k-point sampling.

To study photoexcitation dynamics involving electrons and nuclei, we perform NAQMD simulations.[13−15] The NAQMD method numerically solves time-dependent Kohn−Sham equations in the framework of TDDFT[32] to describe the time evolution of wave functions, subjected to the motions of nuclei through nonadiabatic coupling (NAC). The QXMD code implements a series of methods to efficiently compute interatomic forces incorporating electronic excitations.[33]

Simulated System. A graphene sheet consisting of eight unit cells is obtained through structural optimization, which is placed on a stable (111) surface[22] of a slab of a silicon crystal composed of three atomic double layers, with an interfacial spacing of 4 Å (Figure 1). The lattice constant of silicon in the lateral $x-y$ plane is scaled to match that of the graphene. One carbon atom is placed directly on top of one silicon atom, and centered on these atoms, the entire graphene has 3-fold rotational symmetry along the perpendicular axis to the silicon (111) surface.[22] We adopted this alignment of the interfacial structure because of its high symmetry. The actual experimental results involve many orientations between polycrystalline graphene and silicon,[4] which are expected to be insensitive to a particular alignment. The dangling bonds on the two silicon slab surfaces are terminated with eight hydrogen atoms to stabilize the silicon structure. Vacuum layers, 5 Å each, are added to the top and bottom of the graphene/silicon interface in the surface-normal z direction to prevent interaction between periodic images under the periodic boundary condition. Structural optimization is performed to prepare an initial atomic configuration for the QMD simulation, which is shown in Figure 1. The simulated system consists of 50 atoms, i.e., $\text{Si}_{24}\text{C}_{18}\text{H}_8$. The simulation supercell has the following lattice parameters: $a = 7.4305$ Å, $b = 7.4305$ Å, $c = 22.8505$ Å, $\alpha = 90°$, $\beta = 90°$, and $\gamma = 120°$.

QMD and NAQMD Simulations. Initially, the adiabatic QMD simulation is performed for 10 000 steps with a unit time step Δt of 0.5 fs in the canonical ensemble at 300 K. During the simulation, the atomic positions in the bottom layer of silicon are fixed to represent the bulk silicon crystal. The masses of the hydrogen atoms are made 10 times greater than the physical mass to avoid the use of an extremely small Δt. From the QMD trajectory between 3000 and 10 000 steps, we uniformly sample 29 atomic configurations, which serve as the initial configurations for independent NAQMD simulations for the accumulation of statistics. Here, the charge transfer rate is calculated first by running 29 NAQMD simulations without allowing electron−hole recombination. Subsequently, 29 additional NAQMD simulations are performed using the same initial configurations to calculate the charge recombination rate, where the carriers are allowed to recombine. At the beginning of each NAQMD simulation, an electron is excited from the VBM localized in silicon to the CBM localized in silicon.

In each NAQMD simulation, an electric field E is applied in the z direction to study the response of the graphene/silicon system. The electric field is modeled using a "sawtooth"

potential based on the Berry-phase[19] and double-cell[20] methods.[21] We consider six electric-field strengths (E): −0.0003125, 0, 0.00015625, 0.0003125, 0.000625, and 0.00125 a.u. (in both QMD and NAQMD simulations). An applied electric field gives rise to decreases in potential between silicon and graphene (V_{Gr-Si}), which are computed to be −0.12, 0, 0.06, 0.13, 0.24, and 0.49 V, respectively (see section 2 of the Supporting Information). V_{Gr-Si} values can be directly compared to those in experiments[4] and thus are used in the text instead of electric-field strength E.

■ ASSOCIATED CONTENT

Ⓢ Supporting Information

The Supporting Information is available free of charge at https://pubs.acs.org/doi/10.1021/acs.jpclett.4c02272.

> Profiles of the local Kohn−Sham potential under various electric fields (Figure S1), time evolution of the average occupancies of an excited electron and a hole on silicon and graphene (Figure S2), corresponding standard deviations of the occupancies in Figure S2 (Figure S3), PDOSs and distributions of localized bands at V_{Gr-Si} values of 0 and 0.24 V (Figure S4), a NAQMD simulation in which carrier recombination occurred (Figure S5), charge recombination rates (Figure S6), and correspondence between the applied electric field and voltage (Table S1) (PDF)

■ AUTHOR INFORMATION

Corresponding Authors

Aiichiro Nakano − *Collaboratory for Advanced Computing and Simulation, University of Southern California, Los Angeles, California 90089-0242, United States;* ⊙ orcid.org/0000-0003-3228-3896; Email: anakano@usc.edu

Kohei Shimamura − *Department of Physics, Kumamoto University, Kumamoto 860-8555, Japan;* ⊙ orcid.org/0000-0003-3235-2599; Email: shimamura@kumamoto-u.ac.jp

Authors

Hinata Hokyo − *Collaboratory for Advanced Computing and Simulation, University of Southern California, Los Angeles, California 90089-0242, United States; Department of Physics, Kumamoto University, Kumamoto 860-8555, Japan*

Kai Ito − *Department of Physics, Kumamoto University, Kumamoto 860-8555, Japan*

Rajiv K. Kalia − *Collaboratory for Advanced Computing and Simulation, University of Southern California, Los Angeles, California 90089-0242, United States*

Rehan Kapadia − *Department of Electrical and Computer Engineering, University of Southern California, Los Angeles, California 90089-2560, United States;* ⊙ orcid.org/0000-0002-7611-0551

Fuyuki Shimojo − *Department of Physics, Kumamoto University, Kumamoto 860-8555, Japan;* ⊙ orcid.org/0000-0002-4025-0069

Priya Vashishta − *Collaboratory for Advanced Computing and Simulation, University of Southern California, Los Angeles, California 90089-0242, United States;* ⊙ orcid.org/0000-0003-4683-429X

Complete contact information is available at:
https://pubs.acs.org/10.1021/acs.jpclett.4c02272

Author Contributions

H.H. performed simulations. K.I. and K.S. helped with simulation setup and analysis. F.S. provided simulation techniques. R.K.K., A.N., P.V., and R.K. designed the research. All authors discussed and prepared the manuscript.

Notes

The authors declare no competing financial interest.

■ ACKNOWLEDGMENTS

■ REFERENCES

(1) Dragoman, M.; Dragoman, D. Negative differential resistance in novel nanoscale devices. *Solid-State Electron.* **2022**, *197*, 108464.

(2) Esaki, L. New phenomenon in narrow germanium p-n junctions. *Phys. Rev.* **1958**, *109* (2), 603−604.

(3) Zhu, S.; Sun, B.; Ranjan, S.; Zhu, X.; Zhou, G.; Zhao, H.; Mao, S.; Wang, H.; Zhao, Y.; Fu, G. Mechanism analysis of a flexible organic memristive memory with capacitance effect and negative differential resistance state. *APL Mater.* **2019**, *7* (8), 081117.

(4) Ahsan, R.; Chae, H. U.; Jalal, S. A. A.; Wu, Z.; Tao, J.; Das, S.; Liu, H.; Wu, J.-B.; Cronin, S. B.; Wang, H.; Sideris, C.; Kapadia, R. Ultra-low power in-sensor neuronal computing with oscillatory retinal neurons for frequency-multiplexed, parallel machine vision. *ACS Nano* **2024**, *18* (34), 23785−23796.

(5) Lee, K. W.; Jang, C. W.; Shin, D. H.; Kim, J. M.; Kang, S. S.; Lee, D. H.; Kim, S.; Choi, S.-H.; Hwang, E. Light-induced negative differential resistance in graphene/Si-quantum-dot tunneling diodes. *Sci. Rep.* **2016**, *6* (1), 30669.

(6) Marin, O.; Toranzos, V.; Urteaga, R.; Comedi, D.; Koropecki, R. R. Negative differential resistance in porous silicon devices at room temperature. *Superlattices Microstruct.* **2015**, *79*, 45−53.

(7) Fiori, G. Negative differential resistance in mono and bilayer graphene p-n Junctions. *IEEE Electron Device Lett.* **2011**, *32* (10), 1334−1336.

(8) Britnell, L.; Gorbachev, R. V.; Geim, A. K.; Ponomarenko, L. A.; Mishchenko, A.; Greenaway, M. T.; Fromhold, T. M.; Novoselov, K. S.; Eaves, L. Resonant tunnelling and negative differential conductance in graphene transistors. *Nat. Commun.* **2013**, *4* (1), 1794.

(9) Wang, X.; Wang, Y.; Feng, M.; Wang, K.; Bai, P.; Tian, Y. Light-induced negative differential resistance effect in a resistive switching memory device. *Current Applied Physics* **2020**, *20* (3), 371−378.

(10) Wu, Y.; Farmer, D. B.; Zhu, W.; Han, S.-J.; Dimitrakopoulos, C. D.; Bol, A. A.; Avouris, P.; Lin, Y.-M. Three-terminal graphene negative differential resistance devices. *ACS Nano* **2012**, *6* (3), 2610−2616.

(11) Dominguez, M.; Marquez, E.; Villares, P.; Jimenez-Garay, R. Influence of temperature and interelectrode distance on the negative differential resistance in metal-chalcogenide glassy semiconductors. *J. Mater. Sci.* **1995**, *30* (13), 3407−3414.

(12) Mou, W.; Ohmura, S.; Shimojo, F.; Nakano, A. Molecular control of photoexcited charge transfer and recombination at a quaterthiophene/zinc oxide interface. *Appl. Phys. Lett.* **2012**, *100* (20), 203306.

(13) Craig, C. F.; Duncan, W. R.; Prezhdo, O. V. Trajectory surface hopping in the time-dependent Kohn-Sham approach for electron-nuclear dynamics. *Phys. Rev. Lett.* **2005**, *95* (16), 163001.

(14) Tully, J. C. Perspective: nonadiabatic dynamics theory. *J. Chem. Phys.* **2012**, *137* (22), 22A301.

(15) Shimojo, F.; Hattori, S.; Kalia, R. K.; Kunaseth, M.; Mou, W.; Nakano, A.; Nomura, K.-i.; Ohmura, S.; Rajak, P.; Shimamura, K.;

Vashishta, P. A divide-conquer-recombine algorithmic paradigm for multiscale materials modeling. *J. Chem. Phys.* **2014**, *140* (18), 18A529.

(16) Lin, M. F.; Kochat, V.; Krishnamoorthy, A.; Bassman Oftelie, L.; Weninger, C.; Zheng, Q.; Zhang, X.; Apte, A.; Tiwary, C. S.; Shen, X. Z.; Li, R. K.; Kalia, R.; Ajayan, P.; Nakano, A.; Vashishta, P.; Shimojo, F.; Wang, X. J.; Fritz, D. M.; Bergmann, U. Ultrafast non-radiative dynamics of atomically thin MoSe2. *Nat. Commun.* **2017**, *8*, 1745.

(17) Tung, I.; Krishnamoorthy, A.; Sadasivam, S.; Zhou, H.; Zhang, Q.; Seyler, K. L.; Clark, G.; Mannebach, E. M.; Nyby, C.; Ernst, F.; Zhu, D.; Glownia, J. M.; Kozina, M. E.; Song, S.; Nelson, S.; Kumazoe, H.; Shimojo, F.; Kalia, R. K.; Vashishta, P.; Darancet, P.; Heinz, T. F.; Nakano, A.; Xu, X.; Lindenberg, A. M.; Wen, H. Anisotropic structural dynamics of monolayer crystals revealed by femtosecond surface x-ray scattering. *Nature Photonics* **2019**, *13*, 425–430.

(18) Linker, T.; Nomura, K.; Aditya, A.; Fukshima, S.; Kalia, R. K.; Krishnamoorthy, A.; Nakano, A.; Rajak, P.; Shimmura, K.; Shimojo, F.; Vashishta, P. Exploring far-from-equilibrium ultrafast polarization control in ferroelectric oxides with excited-state neural network quantum molecular dynamics. *Sci. Adv.* **2022**, *8* (12), No. eabk2625.

(19) Umari, P.; Pasquarello, A. Ab initio molecular dynamics in a finite homogeneous electric field. *Phys. Rev. Lett.* **2002**, *89* (15), 157602.

(20) Yarne, D. A.; Tuckerman, M. E.; Martyna, G. J. A dual length scale method for plane-wave-based, simulation studies of chemical systems modeled using mixed ab initio/empirical force field descriptions. *J. Chem. Phys.* **2001**, *115* (8), 3531–3539.

(21) Fukushima, S.; Kalia, R. K.; Nakano, A.; Shimojo, F.; Vashishta, P. Thickness dependence of dielectric constant of alumina films based on first-principles calculations. *Appl. Phys. Lett.* **2022**, *121* (6), 062902.

(22) Sun, Y. W.; Holec, D.; Gehringer, D.; Li, L.; Fenwick, O.; Dunstan, D. J.; Humphreys, C. J. Graphene on silicon: effects of the silicon surface orientation on the work function and carrier density of graphene. *Phys Rev B* **2022**, *105* (16), 165416.

(23) Payne, M. C.; Teter, M. P.; Allan, D. C.; Arias, T. A.; Joannopoulos, J. D. Iterative minimization techniques for ab initio total-energy calculations - molecular-dynamics and conjugate gradients. *Rev. Mod. Phys.* **1992**, *64* (4), 1045–1097.

(24) Mulliken, R. S. Electronic population analysis on LCAO-MO molecular wave functions. 1. *J. Chem. Phys.* **1955**, *23* (10), 1833–1840.

(25) Kawasaki, S.; Kinoshita, K.; Moriya, R.; Onodera, M.; Zhang, Y.; Watanabe, K.; Taniguchi, T.; Sasagawa, T.; Machida, T. Minigap-induced negative differential resistance in multilayer MoS2-based tunnel junctions. *Physical Review Research* **2024**, *6* (3), 033011.

(26) Shimojo, F.; Fukushima, S.; Kumazoe, H.; Misawa, M.; Ohmura, S.; Rajak, P.; Shimamura, K.; Bassman Oftelie, L.; Tiwari, S. C.; Kalia, R. K.; Nakano, A.; Vashishta, P. QXMD: an open-source program for nonadiabatic quantum molecular dynamics. *SoftwareX* **2019**, *10*, 100307.

(27) Hohenberg, P.; Kohn, W. Inhomogeneous electron gas. *Phys. Rev.* **1964**, *136* (3B), B864–B871.

(28) Kohn, W.; Sham, L. J. Self-consistent equations including exchange and correlation effects. *Phys. Rev.* **1965**, *140* (4A), A1133–A1138.

(29) Blochl, P. E. Projector augmented-wave method. *Phys Rev B* **1994**, *50* (24), 17953–17979.

(30) Kresse, G.; Furthmuller, J. Efficient iterative schemes for ab initio total-energy calculations using a plane-wave basis set. *Phys Rev B* **1996**, *54* (16), 11169–11186.

(31) Perdew, J. P.; Burke, K.; Ernzerhof, M. Generalized gradient approximation made simple. *Phys. Rev. Lett.* **1996**, *77* (18), 3865–3868.

(32) Runge, E.; Gross, E. K. U. Density-functional theory for time-dependent systems. *Phys. Rev. Lett.* **1984**, *52* (12), 997–1000.

(33) Shimojo, F.; Ohmura, S.; Mou, W.; Kalia, R. K.; Nakano, A.; Vashishta, P. Large nonadiabatic quantum molecular dynamics simulations on parallel computers. *Comput. Phys. Commun.* **2013**, *184* (1), 1–8.